Copper as promoter of the NiO–CeO$_2$ catalyst in the preferential CO oxidation

Carlos Alberto Chagas [a], Eugenio F. de Souza [a], Robinson L. Manfro [b], Sandra M. Landi [c], Mariana M.V.M. Souza [b], Martin Schmal [a,*]

[a] Núcleo de Catálise, Programa de Engenharia Química, COPPE, Universidade Federal do Rio de Janeiro, Centro de Tecnologia, Bloco G, sala G115, C. P. 68502, CEP 21941-914, Rio de Janeiro, RJ, Brazil
[b] Escola de Química, Universidade Federal do Rio de Janeiro, Centro de Tecnologia, Bloco E, sala 206, CEP 21941-909, Rio de Janeiro, RJ, Brazil
[c] Divisão de Metrologia de Materiais, Instituto Nacional de Metrologia, Qualidade e Tecnologia, Av. Nossa Senhora das Graças 50, 25250-020 Duque de Caxias, Rio de Janeiro, Brazil

A B S T R A C T

This study investigated the influence of the addition of copper on the catalytic performance of the NiO–CeO$_2$ system for preferential CO oxidation reaction (CO–PROX) in hydrogen excess. A systematic structural characterization was performed employing various techniques (XRD, H$_2$-TPR, Raman spectroscopy, HRTEM and XPS) in order to understand the structure–activity relationship. XRD, Raman and HRTEM analysis showed that part of Ni is introduced into the CeO$_2$ structure forming a Ce$_{1−x}$Ni$_x$O$_2$ solid solution and maintaining the fluorite structure, while Cu species added *a posteriori* are dispersed on the ceria surface. The catalytic performance of NiO–CeO$_2$ system was significantly improved by addition of copper. This enhance in CO activity was attributed to synergetic interaction between dispersed copper species and surface oxygen vacancies of ceria support. Conversely, the effect of the presence of copper was not beneficial to the stability. XRD patterns of the catalyst post reaction indicate that metallic Cu and Ni were formed during the course of CO–PROX reaction, while Raman analysis demonstrates the both catalysts presented high resistance to carbon deposition. These results suggest that the decline in CO conversion and CO$_2$ selectivity observed during the stability tests was caused by partial reduction of nickel and copper oxides sites (favored at higher temperatures). In addition, the influence of H$_2$O and CO$_2$ affected severely the reaction rate, however it is totally reversible.

© 2015 Elsevier B.V. All rights reserved.

1. Introduction

Ceria (CeO$_2$) is one of the most important rare-earth oxides and has attracted a lot of interest in the last decades because of its specific properties such as: (i) high oxygen storage capacity (OSC), (ii) good redox performances and (iii) low cost when compared to materials based on noble or precious metals; which makes it very promising for wide range of environmental and energy-related applications [1]. These applications include solid electrolytes in solid oxide fuel cells, oxygen sensors, ultraviolet absorbers, automotive three-way catalysts and catalytic support [2]. Many studies have shown that these redox properties can be considerably enhanced if other metals are introduced into the CeO$_2$ lattice by forming solid solution [3–8]. In addition, CeO$_2$ still shows

the merits in preventing the sintering of metals or oxides dispersed over its surface when applying in catalytic oxidation reaction [9]. It is well established that noble metals supported on CeO$_2$ usually exhibit excellent catalytic performance for oxidation reactions at low temperature, while these supported noble metals are expensive. As consequence, there is a strong demand for development of alternative catalysts with low cost and relatively high activity.

Transition metal oxides including NiO, CuO or Co$_3$O$_4$ have been proposed as promising substitutes because of their low price and catalytic performance comparable to noble or precious catalysts [10]. In particular, Ni-based ceria systems have been the object of numerous publications in the field environmental catalysis, especially because of its catalytic properties in preferential oxidation of CO in excess of H$_2$ (CO–PROX) [9–12]. The literature shows that the activity these catalysts in oxidation reactions is equal or in some cases superior to noble metal based catalysts [10–12]. The favorable performance of Ni-containing systems for catalytic oxidation of CO has been attributed to the increasing concentration of

oxygen vacancies in the ceria crystal structure after Ni doping as well as to the presence of highly dispersed nickel species on its surface [13,14]. However, Ni-containing catalysts have a tendency to catalyze undesired reaction of hydrogenation of CO_2 and CO with consequent formation of methane, besides being prone to coke formation [15]. Importantly, some studies have shown that both the deactivation by coke deposition and the suppression of undesired side reactions can be considerably enhanced if a promoter is introduced along with Ni-based ceria systems [4,16]. Among them, copper (Cu) atoms have a great advantage mainly because of its qualities, such as: catalytic stability, low cost and excellent catalytic performance [8,17–20].

In the last years, many studies have demonstrated the beneficial interaction between nickel and copper [21–24]. These two transition metals have similar crystallographic properties and crystallize in the face-centered cubic (fcc) system with similar lattice parameters of 3.52 Å (Ni) and 3.61 Å (Cu). However, their electronic properties are different: Ni has a partially filled d-band whereas Cu has a completely filled d-band, leading to an electronic interaction that favors the formation of stable Ni–Cu alloys [12,25]. Accordingly, Cu-modified Ni–CeO_2 catalysts have been shown good catalytic performance; besides, it was able to prevent methane formation as well as it presented high resistance to carbon deposition [3,12,15]. According to Saw et al. [12], the improved catalytic performance of Cu-modified NiO–CeO_2 systems might be attributed to the formation of Ni–Cu alloys. Conversely, other studies [8,9,26] suggest that the enhanced activity in CO oxidation and CO_2 selectivity is due to synergistic effect between well-dispersed copper species and surface oxygen vacancies generated via insertion of Ni species in ceria structure. As seen, the precise chemical nature of the resulting interaction between Ni and Cu species in catalytic processes is still an open question in the literature and it is not well understood. Based on the data reported, in this paper we aim at investigating the effect of Cu addition in the improvement of the catalytic performance of NiO–CeO_2 system for CO–PROX reaction. A systematic structural characterization of the catalysts employing various methods (XRD, XPS, Raman, HRTEM and TPR-H_2) was done in order to obtain a close structure-activity correlation.

2. Experimental

2.1. Catalyst preparation

NiO–CeO_2 and CuO–NiO–CeO_2 catalysts were prepared by incipient wetness impregnation method [27]. The nominal loading of NiO and CuO was 20 and 6 wt.%, respectively. The CeO_2 support was obtained by calcination of Ce(NO$_3$)$_3$·6H$_2$O in air at 500 °C for 3 h. Nickel oxide was impregnated on the ceria support with an aqueous solution of the nickel precursor salt (Ni(NO$_3$)$_2$). After impregnation, the sample was dried at 110 °C overnight followed by calcination at 500 °C in air for 3 h to form NiO–CeO_2. The CuO–NiO–CeO_2 catalyst was prepared by sequential impregnation of the NiO–CeO_2 catalyst (the same Ni loading, 20 wt%) with a copper nitrate aqueous solution (Cu(NO$_3$)$_3$). Subsequently, the sample was dried and calcined similarly. From now on the NiO–CeO_2 and CuO–NiO–CeO_2 catalysts are denominated as NiCeO and Cu-modified NiCeO (CuNiCeO), respectively. The 6 wt% CuO/CeO_2 catalyst (from now referred to as CuCeO) prepared by same procedure was used as reference in the catalytic tests.

2.2. Catalyst characterization

Chemical composition analysis of the metal oxides was performed by X-ray fluorescence (XRF) using a Rigaku spectrometer RIX 3100 model apparatus. Nitrogen adsorption/desorption isotherms were obtained at −196 °C using a Micromeritics ASAP2010 gas adsorption instrument. The materials were degassed at 300 °C for 24 h prior to the adsorption experiments. The specific surface areas were calculated using the Brunauer–Emmett–Teller (BET) method.

The X-ray powder diffraction (XRD) measurements were performed using a Rigaku Miniflex diffractometer equipped with a graphite monochromator operated at 30 kV and 15 mA, using CuKα radiation (λ = 1.5406 Å). The measurements were carried out with a step size of 0.05° and counting time of 1 s per step, reproduced here without any background or smoothing treatment. Crystalline structures were refined by Rietveld technique using FULLPROF® 98 code.

High-resolution transmission electron microscopy (HRTEM) and scanning transmission electron microscopy (STEM) images were obtained using an FEI Titan 80-300 microscope operating at 300 kV. The images were acquired using high angle annular dark field (HAADF) detector, providing atomic Z-number contrast. Samples for analysis were prepared by dispersion in water and spread onto a carbon-coated copper grid.

Temperature-programmed reduction (TPR) of the materials was carried out with a 1.53 vol.% H_2/Ar mixture and flow rate of 30 cm^3 min^{-1}. The temperature was increased from room temperature up to 1000 °C. The hydrogen consumption during the reduction was estimated with a thermal conductivity detector (TCD). Prior to TPR analysis, the materials were dried at 150 °C during 1 h under argon flow.

Raman spectra were obtained at room temperature using a LabRam HR-UV800/Jobin–Yvon spectrometer, equipped with a He–Ne laser (λ = 632 nm), thermal conductivity detector (T = −70 °C) and an Olympus BX41 microscope (3–5 regions were analyzed). The surface chemical state of the atoms and their relative abundance were evaluated by X-ray photoelectron spectroscopy (XPS) using an ESCALAB 250 spectrometer (Thermo Scientific), employing monochromatic Al Kα (1486.6 eV) as the X-ray source. The C 1s signal at 284.6 eV was binding energy reference. Spectra were analyzed using a Gaussian–Lorenzian peak shape obtained from CasaXps software.

2.3. Catalytic evaluation

The catalytic tests were carried out in a continuous-flow and fixed-bed microreactor, using 150 mg of catalyst and operating at atmospheric pressure. Prior to reaction, each catalyst was pre-treated in situ with flowing He (60 cm^3 min^{-1}) at 200 °C for 1 h. The reaction was performed at different temperatures from 50 to 200 °C, in steps of 25 °C and kept for 30 min at each temperature. The reaction temperature was measured and controlled by a thermocouple inserted directly into the top of the catalytic bed. The feed composition consisted in 1 vol.% CO, 1 vol.% O_2, 60 vol.% H_2 and He balance at a flow rate of 100 cm^3 min^{-1}. The effect of the water vapor and carbon dioxide on catalytic performances in CO–PROX was also investigated on isothermal conditions at 200 °C. The feed composition for these studies was constituted of 1 vol.% CO, 1 vol.% O_2, 60 vol.% H_2, 10 vol.% CO_2, 3 vol.% H_2O and He balance. Preliminary tests were carried out to eliminate external mass transfer and internal diffusion resistance. Exit gases were analyzed on line using a gas chromatograph system (Trace GC Ultra, Thermo Electron Corp.) equipped with Poraplot Q and molecular sieve columns and TCD and FID detectors. The conversions of CO and O_2 and the CO_2 selectivity were defined by Eqs. (1)–(3) [28]:

$$\text{CO conversion}(\%) = \frac{[CO]_{in} - [CO]_{out}}{[CO]_{in}} \times 100 \qquad (1)$$

Table 1
Physicochemical properties of the materials.

System	Chemical composition (wt%)			S_{BET}	V_p	R_m
	NiO	CuO	CeO$_2$	(m^2 g^{-1})	(cm^3 g^{-1})	(nm)
CeO$_2$ (support)	–	–	100	48	0.205	11.2
NiCeO	18.9	–	81.1	33	0.154	11.05
CuNiCeO	22.2	6.2	71.6	39	0.116	8.76

S_{BET} – specific surface area; V_p – BJH desorption pore specific volume; R_m – BJH desorption average pore radius.
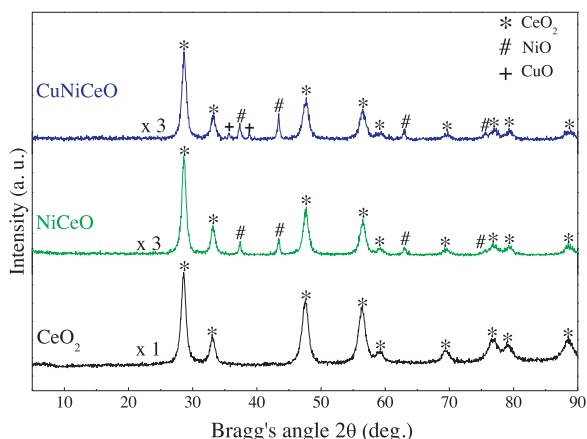

Fig. 1. XRD patterns of the materials.

$$O_2 \text{ conversion}(\%) = \frac{[O_2]_{in} - [O_2]_{out}}{[O_2]_{in}} \times 100 \qquad (2)$$

$$CO_2 \text{ selectivity}(\%) = \frac{0.5 \times [CO_2]_{out}}{[O_2]_{in} - [O_2]_{out}} \times 100 \qquad (3)$$

Equilibrium compositions were calculated by the minimization of the Gibbs free energy. The calculations were done for products as a function of temperature, pressure and composition, based on the Lagrange multipliers principle and ideal gas hypothesis. All the catalytic tests were carried out in triplicates and the values obtained for CO conversion showed a standard deviation below 3.0%.

3. Results and discussion

3.1. Specific surface area (BET), X-ray diffraction (XRD) and Raman analysis

The N$_2$ adsorption–desorption isotherms are shown in Fig. S1 (see in Supplementary information, SI). As seen, all isotherms exhibited common features and are similar in shape to the type-IV with H1 hysteresis loops, revealing the mesoporous nature of the materials [29]. Some textural properties are reported in Table 1.

The decrease observed for mesoporous volume (from 0.205 to 0.116 cm^3 g^{-1}) and pore radius (from 11.2 to 8.76 nm) was assigned to the blocking of pores upon Ni/Cu incorporation, which in turn might be limiting the accessibility of adsorbing molecules. Similar phenomenon has been observed in other studies [13,17,18]. Furthermore, the XRF chemical analysis (Table 1) shows Ni, Cu and Ce amounts close to the nominal composition.

The XRD patterns (Fig. 1) shows well-resolved peaks indicating the crystalline nature of the materials. As can be observed, the peaks related to pure ceria agrees well with those expected for cubic (fluorite-type) CeO$_2$ structure (JCPDS 34-0394) and no other diffraction peaks due to impurities or precursors were detected. On the other hand, the XRD patterns of NiCeO and CuNiCeO also include peaks corresponding to NiO phase (JCPDS 44-1159). However, the presence of NiO diffraction lines does not exclude the formation of solid solutions *via* incorporation of part of Ni into the CeO$_2$ structure, as will be discussed later. Importantly, two less intense peaks relative to CuO phase (JCPDS 48-1548) can also be seen at 35–40° in the XRD pattern of the CuNiCeO system, suggesting that these species are small and highly dispersed on ceria surface.

The solid solution formation of the type Ce$_{1-x}$Ni$_x$O$_2$ was checked by estimation of the lattice parameter obtained *via* structural refinement of the XRD patters using Rietveld methodology. The results are depicted in Fig. 2 and show a very good correspondence between experimental data and simulated curves, confirmed by observing the difference patterns. Some structural properties inferred by Rietveld refinement are summarized in Table 2. The results revealed a decrease in the lattice parameter from 5.413 Å in pure ceria to 5.407 Å in both NiCeO and CuNiCeO systems, suggesting that part of the Ni species has been inserted into the ceria structure. In principle, the cell contraction observed could be assigned to the smaller size of Ni^{2+} ions (0.72 Å) when compared with Ce^{4+} ions (0.97 Å), which in turn would imply in the formation of a Ce$_{1-x}$Ni$_x$O$_2$ solid solution [26] On the other hand, Cu added *a posteriori* and remaining Ni (which have not been incorporated) are believed to form segregated phases CuO and NiO, respectively, as evidenced by our XRD patterns. Moreover, no significant changes in the mean crystallite size were observed (Table 2).

The formation of solid solution is also supported by Raman experiments, as presented in Fig 3. All spectra show a main band
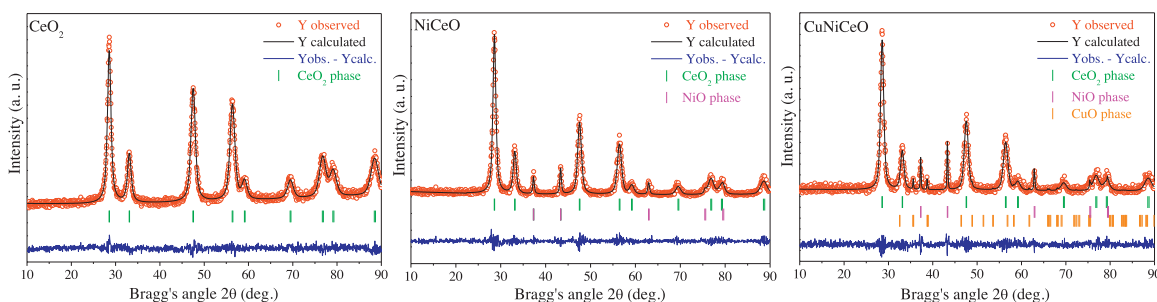

Fig. 2. Rietveld refinement of the XRD patterns. Experimental data are indicated by red circles while the refined values form the continuous black line. The difference between the experimental and calculated curves is represented by the lowest blue line(For interpretation of the references to colour in this figure legend, the reader is referred to the web version of this article.)

Table 2
Cell parameters and mean crystal size of the materials obtained by Rietveld refinament.

System	Cell parameter (Å)	Crystal size (Å)[a]		
	a = b = c (CeO_2)	CeO_2	NiO	CuO
CeO_2 (support)	5.413	93	–	–
NiCeO	5.407	104	253	–
CuNiCeO	5.407	102	285	293

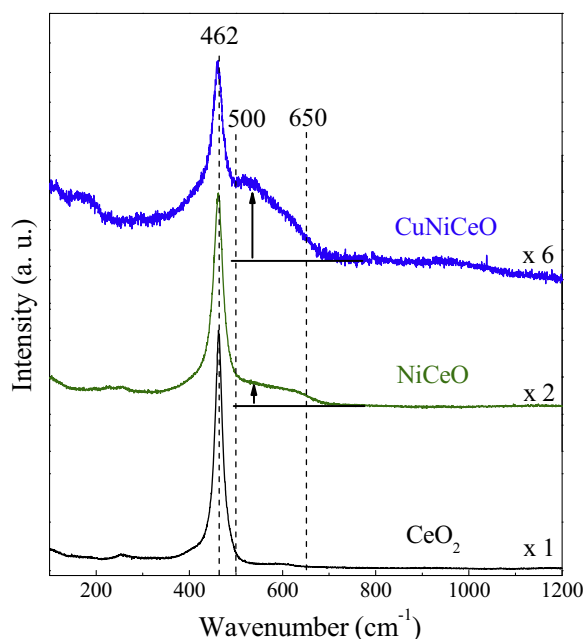[a] Calculated using Scherrer equation to the most intense peak of the corresponding specie.

Fig. 3. Raman spectra of the materials.

Fig. 4. TPR profiles of the materials.

around $462 \, cm^{-1}$, which corresponds to the triply degenerate F_{2g} mode of fluorite CeO_2 [8]. The appearance of a broad band ranging from 500 to $650 \, cm^{-1}$ was observed after the incorporation of nickel and copper and can be attributed to the presence of oxygen vacancies created in the ceria structure [8,17], since the incorporation of part of the Ni^{2+} ions into the CeO_2 structure to replace some Ce^{4+} ions must be accompanied by generation of oxygen vacancies in order to maintain the charge neutrality ($Ce^{4+} + O^{2-} \rightarrow Ni^{2+} + v_0$; being $v0$ doubly ionized oxygen vacancy). Thus, our Raman and XRD results are in good agreement providing additional evidence of $Ce_{1-x}Ni_xO_2$ solid solution formation.

3.2. Temperature Programmed Reduction (TPR) studies

TPR experiments were performed in order to examine the influence of reducing atmosphere (as in our catalytic tests) as well as to offer more information about the chemical interactions between Ni and Cu species and ceria. The reduction profiles are shown in Fig. 4. Pure CeO_2 displays two reduction peaks at 455 and 555 °C, ascribed to the reduction of surface cerium ($Ce^{4+} \rightarrow Ce^{3+}$) and another peak around 945 °C attributed to the reduction in the bulk phase [1,30]. The reduction profiles of NiCeO and CuNiCeO systems were found to be more complex mainly because of the incorporation of Ni into the ceria lattice, as discussed previously. Thus, in order to get a deeper insight about the reduction process the H_2-consumption peaks have been fitted through a Gaussian model. From Fig. 4, one can see that NiCeO displayed four H_2 consumption peaks, besides a reduction peak at 977 °C relative to ceria. Furthermore, the two major H_2 consumption peaks at 390 and 465 °C can be assigned to the reduction of small and larger NiO particles (NiO $\rightarrow$ Ni^0),
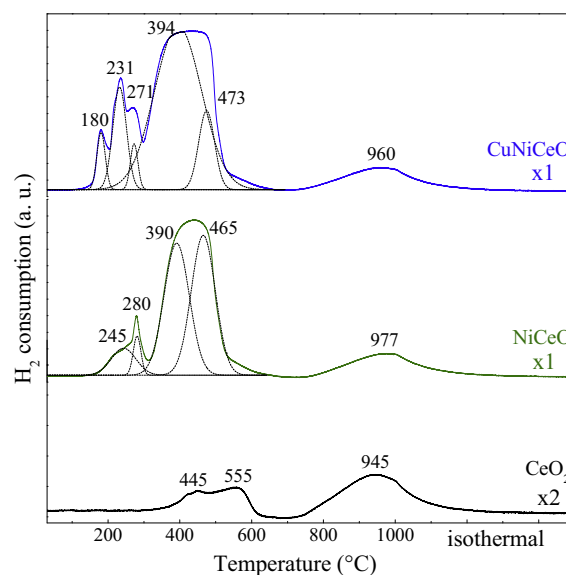
respectively, suggesting different degrees of interaction with the support [31–33]. Interestingly, two overlapping reduction peaks centered at lower temperatures (245 and 280 °C) were also observed. The first peak at 245 °C can be attributed to the reduction of O_2 molecules possibly adsorbed on surface oxygen (O) vacancies [26,34]; as discussed in Section 3.1, the incorporation of Ni species into the ceria lattice usually generates O vacancies that can easily adsorb O_2 molecules, which in turn can be easily reduced by H_2 at lower temperatures. The second peak located at 280 °C corresponds to the reduction of Ni species present into the CeO_2 lattice [26].

On the other hand, the Cu-modified system (CuNiCeO) exhibited one more reduction peak at lower temperature (180 °C) which can be assigned to the reduction of Cu species dispersed over the CeO_2 surface [5]. Some studies demonstrate that Cu species interacting with ceria can be reduced at a relatively lower temperature when compared to the reduction of copper ions in CuO [5,12]. Regarding CuNiCeO, the reduction of the Cu species detected by XRD patterns (see Fig. 1) occurred probably at temperatures below 300 °C although concomitantly with nickel species. From Fig 4 can be seen that on CuNiCeO system peak below 300 °C is more intense than those of NiCeO, probably due to copper reduction contribution. There is an overlapping of the reduction peaks of nickel, copper and surface cerium species on the NiCeO and CuNiCeO systems in the temperature range between 100 and 600 °C (see Fig. 4), showing that the reduction of each component is influenced by the reduction of surface CeO_2 species, and that makes difficult the quantitative analyses. Thus, considering the reduction of NiCeO and CeO_2 in Fig. 4 and discounting the reduction of surface CeO_2 we observed a reduction degree of 95% of nickel in this system. More difficult is the analysis of the CuNiCeO system. In fact, Fig. S2 (SI) displays the TPR profile of the CuCeO system and one observe a experimental H_2 consumption of Cu species (115 μmol) higher than needed for the
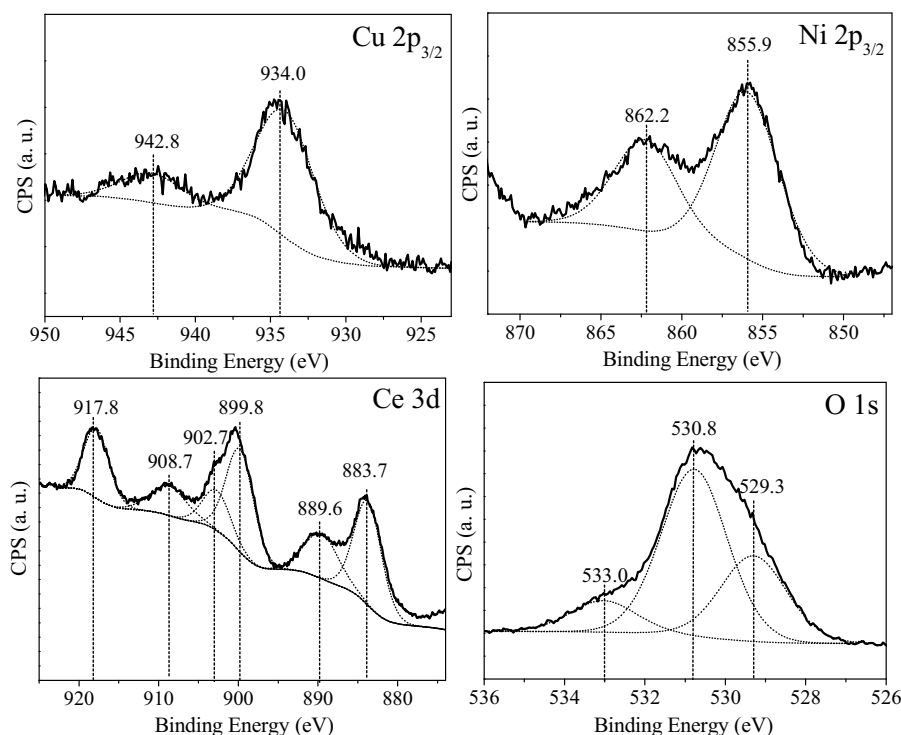
Fig. 5. XP spectra of the CuNiCeO system.

reduction of CuO (77 μmol of H_2), which indicates that the reduced Cu catalyzes significantly the reduction of CeO_2. The same behavior was observed on the CuNiCeO system whose experimental H_2 consumption (416 μmol) was higher which the necessary for reducing of NiO and CuO (305 and 85 μmol of H_2, respectively), reinforcing that both Cu and Ni increased the reduction of CeO_2.

3.3. X-ray photoelectron spectroscopy (XPS) studies

The surface species were investigated by XPS analysis and the XP spectra of Ni 2p, Cu 2p, Ce 3d, O 1 s and C 1 s regions for CuNiCeO is given in Fig. 5. The spectrum of nickel exhibited a main peak around 855.9 eV corresponding to the Ni $2p_{3/2}$ line, followed by a relatively intense shake up satellite peak around 862.2 eV, characteristics of Ni^{2+} species in the form of NiO [35]. The spectrum relative to the Cu $2p_{3/2}$ region showed two peaks associated to the $2p_{3/2}$ line and shake up satellite at 934.0 and 942.8 eV, respectively, indicating that only Cu^{2+} species as CuO were present on the CuNiCeO surface [36]. The complex spectrum of Ce 3d was decomposed into six contributions. The peaks located at 883.7, 889.6 and 899.8 eV are ascribed to the Ce $3d_{5/2}$ line, whereas the peaks at 902.7, 908.7 e 917.8 eV correspond to the Ce $3d_{3/2}$ line. This result suggests that the Ce existed on the CuNiCeO surface mainly as Ce^{4+} [37]. These findings indicate a similar oxidation state of the atoms on surface and in the bulk (as evidenced by XRD analysis) and exclude the existence of metallic species in the CuNiCeO system. The spectrum of O 1 s was fitted to three components, the one positioned at high binding energy (533.0 eV) characteristic of carbonate structures and a prominent one around 530.8 eV due to the presence of hydroxyl groups. Another visible component is found at a binding energy of 529.3 eV. This peak is relative to the oxygen vacancies in ceria, in accordance with XRD and Raman analysis [13]. The XP spectra of NiCeO are illustrated in Fig. S3 (SI). No significant differences of theses spectra compared to the XPS spectra of the CuNiCeO system (Fig. 5) was observed, except in relation to the presence of copper.

3.4. Transmission electron microscopy (TEM/STEM) studies

To complement the structural analysis, NiCeO and CuNiCeO systems were examined by microscopy and the representative TEM images are shown in Fig. 6. The images reveal a microstructural similarity for both systems, displaying clearly lattice fringes typical of highly crystalline materials. Fig. 7 displays a HRTEM micrograph in higher magnification showing detailed structure of the CuNiCeO. Fast Fourier transformation (FFT) was applied in order to calculate the lattice spacing of the crystallites. The existence of two distinct domains, corresponding to CeO_2 and NiO phases, is clearly visible. The FFT images of the CeO_2 particles (Fig. 7b) exhibited visible lattice spacing in its structure compatible with the reflection planes of the ceria phase. Fig. S4 (SI) shows images of the CuNiCeO system acquired in TEM and HAADF-STEM modes. The presence of small pores (8–9 nm) is clearly visible in the images. This is in excellent agreement with the average pore radius estimated by N_2 isotherm (8.7 nm), as previously shown in Table 1. The elemental distribution map of the CuNiCeO system is presented in Fig. S5a–d (SI). The EDX mapping image reinforces our assumption that Cu (Fig. S5b) is relatively well distributed in the agglomerate. In contrast, it is possible verify the existence of domains of Ni (Fig. S5a) due to its relatively non-uniform distribution. This observation becomes more evident when the elemental maps of Ce (red), Cu (blue) and Ni (green) are combined (overlapping), as illustrated in Fig. S5e (SI). It is possible to identify more easily regions of the particle with relative concentration of Cu, and the regions enriched in Ni.

3.5. Catalytic tests

The CO conversion as a function of the reaction temperature is shown in Fig. 8a. For comparison, the catalytic activity of the CuCeO system (catalyst reference) was also included. As seen, the CO conversion increase by raising the temperature, attaining maxima located at 100, 125 and 175 °C for CuCeO, CuNiCeO and NiCeO, respectively. On the other hand, the activity of the CeO_2 support
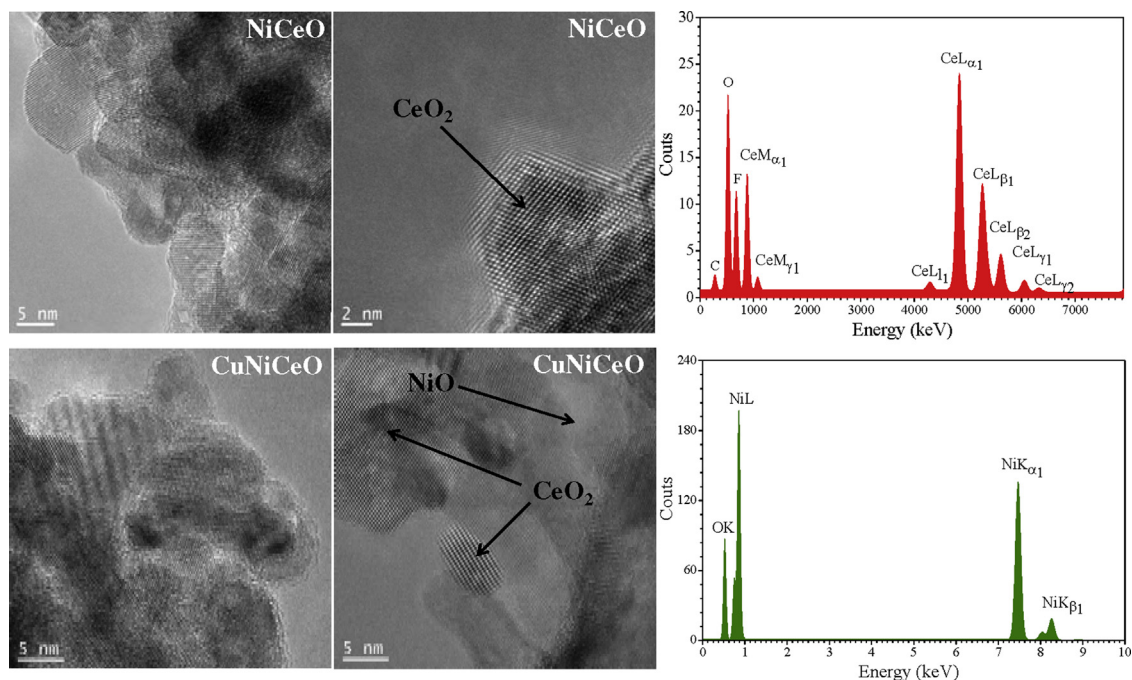
Fig. 6. Representative TEM images of the systems and EDX spectra acquired on CeO_2 (upper one) and NiO (lower one).
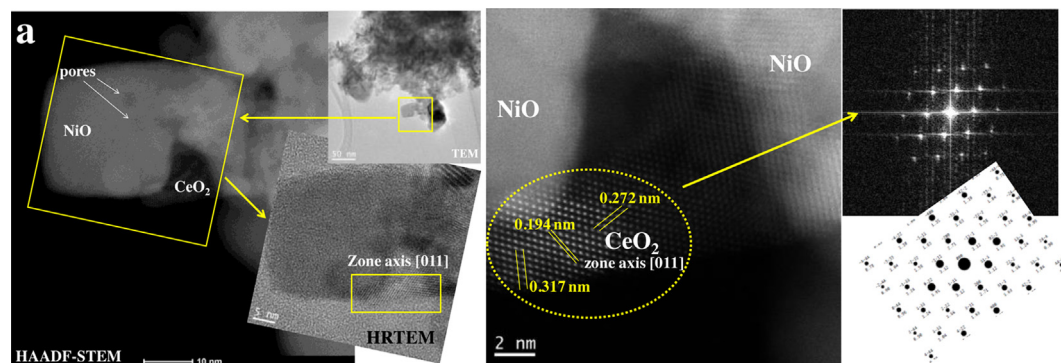

Fig. 7. High magnification TEM/STEM images of the CuNiCeO system and corresponding FFT and simulation of the crystal structure (CrystalKitX version 1.9.3).
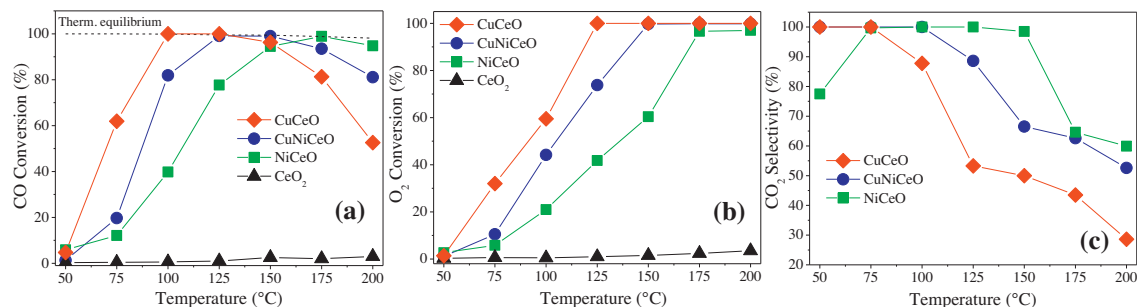

Fig. 8. CO conversion (a), O_2 conversion (b) and CO_2 selectivity (c) as a function of the reaction temperature.

was low (below 5.0 %). The catalytic activity can be usually associated with the temperature corresponding to 50% of CO conversion to CO_2 ($T_{50\%CO}$). In our case, $T_{50\%CO}$ values were obtained from the light-off curve [38] and are summarized in Table 3. The results show that the reference catalyst CuCeO was the most active compared to the NiCeO and CuNiCeO, however, the simple addition of copper on the NiCeO system induced a significant reduction of $T_{50\%CO}$, from 107 to 88 °C. Indeed, the superior activity of CuNiCeO

can be attributed to the presence of dispersed copper species, as shown in the reference test of the CuCeO catalyst. In fact, there is a synergistic interaction between Cu and O vacancies, which are responsible for the generation of highly active sites on the copper/ceria interface, thus enhancing the chemical activity of these systems, as reported by Wang et al. [39]. A similar effect has been reported by Gamarra et al. [8] and also attributed to the dispersed copper species interacting strongly with ceria. However, in a recent

Table 3
Light-off temperatures for CO–PROX reaction.

System	CO conversion		CO₂ selectivity (%)
	$T_{50\%CO}$ (°C)[a]	T_{max} (°C)[b]	
NiCeO	107	175	100
CuNiCeO	88	125	100
CuCeO	70	100	100

[a] $T_{50\%CO}$: temperature at which 50% of CO was converted.

[b] T_{max} : temperature corresponding to the maximum CO conversion reached in the CO–PROX reaction

work Saw et al. [12] proposed that a bimetallic Ni-Cu alloy, identified in a Ni-Cu/CeO₂ based system, is the main active site for CO adsorption. According to Rodriguez and Goodman [40], the generation of a hetero-nuclear Ni–Cu bond modifies the electronic level, altering the chemical properties of the alloy. Nevertheless, Ni–Cu interaction was not observed in this system using different characterization techniques, although it did not necessarily preclude the formation this alloy.

On the other hand, there is a substantial decrease in the CO conversion (see Fig. 8a) at high temperatures (above 150 °C), which is more pronounced for the reference catalyst CuCeO. Fig. 8b shows that the O₂ conversion for the catalysts, following the same tendency, reaching a total conversion at 125, 150 and 175 °C for CuCeO, CuNiCeO and NiCeO, respectively. Total O₂ consumption at higher temperatures was accompanied by a significantly drop in CO conversion. As the CO/O₂ ratio employed in the reactant mixture is 1/1 (representing an O₂ concentration higher than that stoichiometrically required, *i.e.* 1/0.5), it indicates the occurrence of a side reaction (H₂ oxidation). In addition, the formation of H₂O (verified during our catalytic test) was more significant when O₂ was completely consumed, evidencing an increase in H₂ oxidation. Similar findings were previously reported by our group [28,41]. CO₂ selectivity profiles shown in Fig 8c exhibited similar behavior; however the initial CO₂ selectivity of CuNiCeO was 100% (75 °C), whereas for NiCeO it is around 78% (50 °C). The CO₂ selectivity of CuCeO decreased sharply. Moreover, an appreciable formation of CH₄ was detected, which is ascribed to the promotion of the methanation reaction (favored at higher temperatures). Similar observations have been reported in the literature [10,15,28,41]. In addition, the CH₄ formation occurs mainly on metallic nickel, whereas metallic copper species are favor the WGS reaction. Thus, the partial reduction of the oxide during the reaction inhibits the oxidation of CO favoring the methanation and shift reactions.

The stability of the catalysts was tested with time on stream at 200 °C for 30 h. As seen in Fig. S6 (SI), the NiCeO and CuCeO catalysts are very stable during 30 h without significant deactivation, while
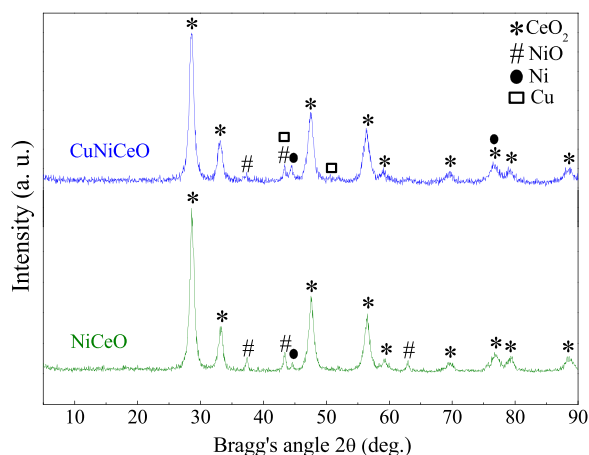

Fig. 9. XRD patterns of the used systems.

the CO conversion on CuNiCeO decreased up to 10 h (from 81 to 69%).

3.6. Post-reaction analyses

After reaction the catalysts were analyzed by Raman and XRD. The Raman spectra are displayed in Fig. S7 (SI) and do not evidence carbonaceous species at the surfaces, as shown in the high wavenumber region (between 900 and 1800 cm⁻¹), (absence of D and G bands) suggesting that these catalysts are resistant to carbon deposition under these experimental conditions. Furthermore, additional diffraction peaks at 43.3 and 44.5° in the XRD patterns of the used catalysts (Fig. 9) were observed, which can be attributed to the metallic Cu and Ni, respectively. The appearance of these peaks was accompanied by a decreasing intensity of peaks relative to the NiO and CuO phases, evidencing its partial reduction during the course of reaction. These results suggest that the presence of both metallic species is, in principle, responsible for the drop observed in the CO conversion. In addition, the partial reduction of NiO phase was more pronounced on the CuNiCeO catalyst after use. According to the literature the metallic cobalt, as well as nickel sites are less active for CO oxidation, but very active for the methanation and H₂ oxidation reactions [42], in agreement with our findings. The Rietveld refinement of the XRD patterns of the catalysts after reaction is presented in Fig. 10, and the quantitative estimation of crystallite sizes is summarized in Table S1 (SI). No significant changes of the crystallite sizes of NiO and CeO₂ during the reaction were observed, indicating that the deactivation observed in Fig. S6 (SI) was not caused by structural modification
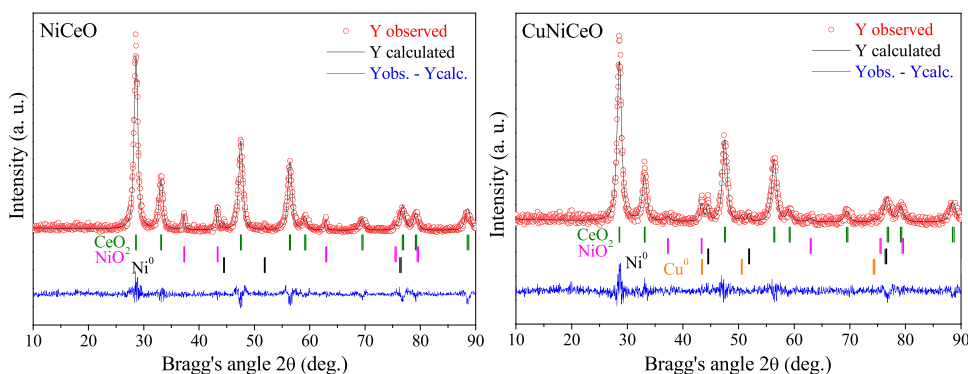

Fig. 10. Rietveld refinement of the XRD patterns of the used systems. Experimental data are indicated by red circles and the calculated values by refinement form the continuous black line. The difference between the experimental data and the calculated curve is represented by the lowest blue line(For interpretation of the references to colour in this figure legend, the reader is referred to the web version of this article.)
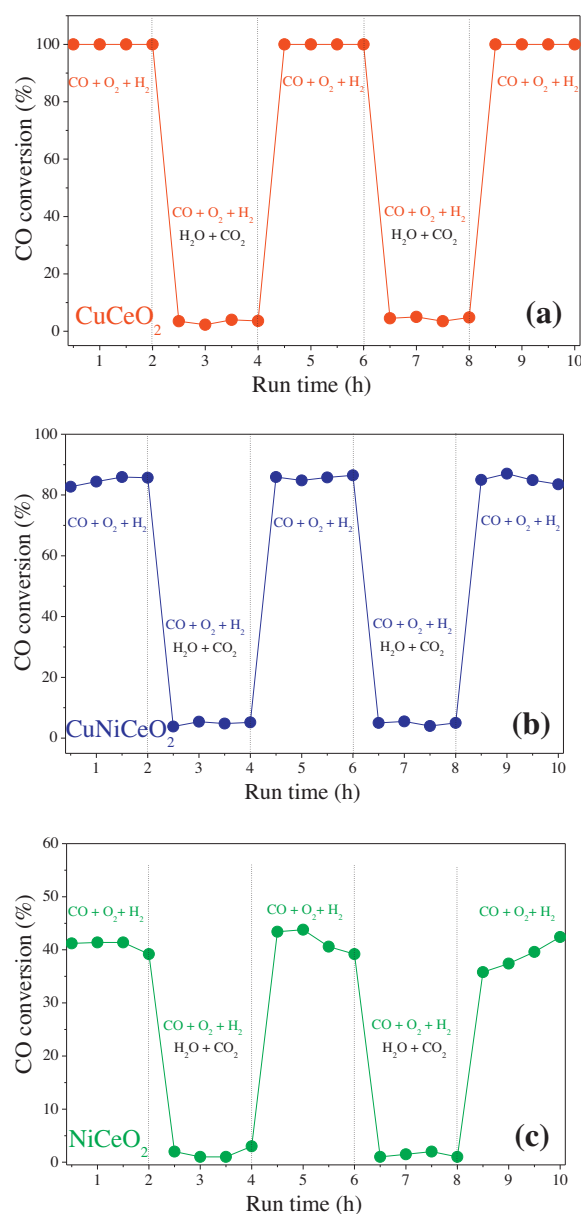
Fig. 11. Effect of the 3 vol.% H_2O and 10 vol.% CO_2 addition in the gas feed at 200 °C. Systems: (a) CuCeO, (b) CuNiCeO and (c) NiCeO.

(sintering). Thus, based on these results we may infer that the deactivation is attributed to the formation of metallic Ni and Cu sites during CO–PROX reaction due to the partial reduction of copper and nickel oxides. These sites catalyze undesired side reaction like H_2 oxidation, causing the drop in the CO activity and CO_2 selectivity.

3.7. The effect of CO_2 and H_2 during reaction

These components are the main products of the reaction and of the feed resulting from the WGSR which may affect the reaction rate. Thus, the effect of the presence of CO_2 and H_2O in the feed reaction mixture was studied in the CO–PROX reaction in order to evaluate the catalytic performance in more realistic reaction conditions. The reaction was performed by adding simultaneously CO_2 and H_2O in the feed stream at 200 °C for all catalysts without any pretreatment, and results are displayed in Fig. 11. Results show that the initial conversion of CO of the CuCeO system decreased from 100% to less than 10% after alternative or simultaneous switching to H_2O and CO_2 in the feed mixture, during the reaction under

similar conditions. Similarly, the conversions of CuNiCeO and NiCeO decayed from 90 and 45% to less than 5%, respectively. Interesting is that, when CO_2 and H_2O are removed from the feed gas, the initial CO conversion of all catalysts was almost recovered. These results show that the presence of CO_2 and H_2O influence the reaction affecting the CO conversion, poisoning the active sites. Since these are products of the reaction probably they may inhibit the reaction kinetics for concentrations above the feed level, but not on the structure of the surface active sites because the conversion is fully restored. This negative effect could be due to a competitive adsorption on the active sites [43], and/or to the formation of carbonate groups on the catalyst surface [44,45].

4. Conclusions

The influence of the addition of copper on the catalytic performance of the NiO–CeO$_2$ system for preferential CO oxidation reaction (CO–PROX) in H_2-rich stream has been studied. Our study demonstrates that the CO oxidation activity of NiO–CeO$_2$ system was significantly improved by addition of copper. This result can be attributed to the synergetic interaction between copper species finely dispersed and oxygen vacancies created *via* incorporation of Ni into ceria structure, as evidenced by our characterization results. Raman experiments corroborate the formation of defects and oxygen vacancies, which are responsible for favoring lattice oxygen mobility. Conversely, the effect of the presence of copper was not beneficial to the stability. XRD patterns of the catalyst post reaction indicate that metallic Cu and Ni were formed during the course of CO–PROX reaction, while Raman analysis demonstrates the both catalysts presented high resistance to carbon deposition. These results suggest that the decline in CO conversion and CO_2 selectivity observed during the stability tests was caused by partial reduction of copper and nickel oxides sites (favored at higher temperatures). The influence of H_2O and CO_2 affected severely the reaction rate, however it is totally reversible. These results show that the presence of CO_2 and H_2O poisons the active sites, inhibiting the reaction kinetics for concentrations above the feed level, but not on the structure of the surface active sites because the conversion is fully restored. This negative effect could be due to a competitive adsorption on the active sites, and/or to the formation of carbonate groups on the catalyst surface.

Appendix A. Supplementary data

Supplementary data associated with this article can be found, in the online version, at http://dx.doi.org/10.1016/j.apcatb.2015.09.033.

References

[1] C.A. Chagas, L.C. Dieguez, M. Schmal, Catal. Lett. 142 (2012) 753–762.
[2] B. Lu, K. Kawamoto, Mater. Res. Bull. 53 (2014) 70–78.
[3] Y. Liu, K. Murata, M. Inaba, I. Takahara, K. Okabe, Fuel 104 (2013) 62–69.
[4] Z. Wang, Z. Qu, X. Quan, Z. Li, H. Wang, R. Fan, Appl. Catal. B Environ. 134–135 (2013) 153–166.
[5] P. Bera, K.R. Priolkar, P.R. Sarode, M.S. Hegde, S. Emura, R. Kumashiro, et al., Chem. Mater. (2002) 3591–3601.
[6] B. Solsona, P. Concepción, S. Hernández, B. Demicol, J.M.L. Nieto, Catal. Today 180 (2012) 51–58.
[7] S. Xu, X. Yan, X. Wang, Fuel 85 (2006) 2243–2247.

[8] D. Gamarra, G. Munuera, A.B. Hungrı, M. Fernández-Gracia, J.C. Conesa, P.A. Midgley, X.Q. Wang, et al., J. Phys. Chem. C 111 (2007) 11026–11038.
[9] X. Liu, Y. Zuo, L. Li, X. Huang, G. Li, RSC Adv. 4 (2014) 6397.
[10] J.A. Gómez-Cuaspud, M. Schmal, Int. J. Hydrogen Energy 38 (2013) 7458–7468.
[11] P.Y. Peng, I. Jin, T.C.K. Yang, C.M. Huang, Chem. Eng. J. 251 (2014) 228–235.
[12] E.T. Saw, U. Oemar, X.R. Tan, Y. Du, A. Borgna, K. Hidajat, et al., J. Catal. 314 (2014) 32–46.
[13] S. Mahammadunnisa, M.K. Reddy, N. Lingaiah, S. Ch, Catal. Sci. Technol. 3 (2013) 730–736.
[14] T. Li, G. Xiang, J. Zhuang, X. Wang, Chem. Commun. (Camb) 47 (2011) 6060–6062.
[15] A. Jha, D.-W. Jeong, W.-J. Jang, C.V. Rode, H.-S. Roh, RSC Adv. 5 (2015) 1430–1437.
[16] P. Larsson, A. Andersson, Appl. Catal. B Environ. 24 (2000) 175–192.
[17] D. Gamarra, A.L. Cámara, M. Monte, S.B. Rasmussen, L.E. Chinchilla, A.B. Hungría, et al., Appl. Catal. B Environ. 130–131 (2013) 224–238.
[18] J.L. Ayastuy, A. Gurbani, M.P. González-Marcos, M.A. Gutiérrez-Ortiz, Int. J. Hydrogen Energy 35 (2010) 1232–1244.
[19] T.S. Mozer, F.B. Passos, Int. J. Hydrogen Energy 36 (2011) 13369–13378.
[20] P. Zhu, J. Li, S. Zuo, R. Zhou, Appl. Surf. Sci. 255 (2008) 2903–2909.
[21] A. Hornés, M.J. Escudero, L. Daza, A. Martínez-Arias, J. Power Sources 249 (2014) 520–526.
[22] A. Hornés, P. Bera, M. Fernández-García, A. Guerrero-Ruiz, A. Martínez-Arias, Appl. Catal. B Environ. 111–112 (2012) 96–105.
[23] Y. Park, S.K. Kim, D. Pradhan, Y. Sohn, Chem. Eng. J. 250 (2014) 25–34.
[24] G. Chen, Q. Li, Y. Wei, W. Fang, Y. Yang, Chin. J. Catal. 34 (2013) 322–329.
[25] G. Ranga Rao, S.K. Meher, B.G. Mishra, P.H.K. Charan, Catal. Today 198 (2012) 140–147.
[26] A. Vita, L. Pino, F. Cipitì, M. Laganà, V. Recupero, Fuel Process Technol. 127 (2014) 47–58.
[27] K. Lertwittayanon, D. Atong, P. Aungkavattana, T. Wasanapiarnpong, S. Wada, V. Sricharoenchaikul, Int. J. Hydrogen Energy 35 (2010) 12277–12285.
[28] C.A. Chagas, F.S. Toniolo, R.N.S.H. Magalhães, M. Schmal, Int. J. Hydrogen Energy 37 (2012) 5022–5031.
[29] G. Leofanti, M. Padovan, G. Tozzola, B. Venturelli, Catal. Today 41 (1998) 207–219.
[30] V.D. Araújo, J.D.A. Bellido, M.I.B. Bernardi, J.M. Assaf, E.M. Assaf, Int. J. Hydrogen Energy 37 (2012) 5498–5507.
[31] I. Luisetto, S. Tuti, E. Di Bartolomeo, Int. J. Hydrogen Energy 37 (2012) 15992–15999.
[32] Y. Wang, A. Zhu, Y. Zhang, C.T. Au, X. Yang, C. Shi, Appl. Catal. B Environ. 81 (2008) 141–149.
[33] X. Du, D. Zhang, L. Shi, R. Gao, J. Zhang, J. Phys. Chem. C 116 (2012) 10009–10016.
[34] L. Pino, A. Vita, F. Cipitì, M. Laganà, V. Recupero, Catal. Lett. 122 (2008) 121–130.
[35] M.A. Peck, M.A. Langell, Chem. Mater. 24 (2012) 4483–4490.
[36] X. Zhang, J. Zhou, H. Song, X. Chen, Y.V. Fedoseeva, A.V. Okotrub, et al., Appl. Mater. Interfaces 6 (2014) 17236–17724.
[37] B.M. Reddy, A. Khan, Y. Yamada, T. Kobayashi, S. Loridant, J.-C. Volta, J. Phys. Chem. B 107 (2003) 5162–5167.
[38] M. Haruta, N. Yamada, T. Kobayahsi, S. Lijima, J. Catal. 115 (1989) 301–309.
[39] X. Wang, J.A. Rodriguez, J.C. Hanson, D. Gamarra, A. Martínez-Arias, M. Fernández-García, J. Phys. Chem. B 110 (2006) 428–434.
[40] J.A. Rodriguez, D.W. Goodman, Science 257 (1992) 897–903.
[41] M. Schmal, C.A. Perez, R.N.S.H. Magalhães, Top. Catal. 57 (2014) 1103–1111.
[42] M.P. Woods, P. Gawade, B. Tan, U.S. Ozkan, Appl. Catal. B Environ. 97 (2010) 28–35.
[43] R.J.H. Grisel, B.E. Nieuwenhuys, J. Catal. 199 (2001) 48–59.
[44] S. Monyanon, S. Pongstabodee, A. Luengnaruemitchai, J. Power Sources 163 (2006) 547–554.
[45] M. Daté, M. Okumura, S. Tsubota, M. Haruta, Angew. Chem. Int. Ed. 43 (2004) 2129–2132.